Journal of Materials Science & Technology 35 (2019) 1532–1542

Contents lists available at ScienceDirect

Journal of Materials Science & Technology

journal homepage: www.jmst.org

Constructing two-scale network microstructure with nano-Ti_5Si_3 for superhigh creep resistance

Y. Jiao [a,b], L.J. Huang [a,*], S.L. Wei [c], H.X. Peng [d], Q. An [a], S. Jiang [a], L. Geng [a]

[a] State Key Laboratory of Advanced Welding and Joining, Harbin Institute of Technology, Harbin 150001, China
[b] Center of Analysis and Measurement, Harbin Institute of Technology, Harbin 150001, China
[c] Department of Materials Science and Engineering, Massachusetts Institute of Technology, Cambridge, MA02139, USA
[d] Institute for Composites Science Innovation (InCSI), School of Materials Science and Engineering, Zhejiang University, Hangzhou 310027, China

ARTICLE INFO

Article history:
Received 3 September 2018
Received in revised form 3 November 2018
Accepted 22 March 2019
Available online 5 April 2019

Keywords:
Titanium matrix composite
Two-scale network microstructure
Nano-Ti_5Si_3
Creep
Powder metallurgy

ABSTRACT

The improvement of mechanical properties must be achieved by designing and constructing more suitable microstructure, such as hierarchical microstructure. In order to significantly enhance the creep resistance of titanium matrix composites (TMCs), two-scale network microstructure was constructed including the first-scale network (<150 μm) with micro-TiB whisker (TiBw) reinforcement and the second-scale network (<30 μm) with nano-Ti_5Si_3 reinforcement by powder metallurgy and in-situ synthesis. The results showed that the creep rate of the composite was remarkably reduced by an order of magnitude compared with the Ti6Al4V alloy at 550 °C, 600 °C, 650 °C under the stresses between 100 MPa and 350 MPa. Moreover, the rupture time of the composite was increased by 20 times, compared with that of the Ti6Al4V alloy at 550 °C/300 MPa. The superior creep resistance could be attributed to the hierarchical microstructure. The micro-TiBw reinforcement in the first-scale network boundary contributed to creep resistance primarily by blocking grain boundary sliding, while the nano-Ti_5Si_3 particle in the second-scale network boundary mainly by hindering phase boundary sliding. In addition, the nano-Ti_5Si_3 particle was dissolved, and precipitated with smaller size than the primary Ti_5Si_3. This phenomenon was attributed to Si element diffusion under high temperature and external stress, which could further continuously enhance the creep resistance. Finally, the creep rate during steady-state stage was significantly decreased, which manifested superior creep resistance of the composite.

1. Introduction

Titanium (Ti) alloys are unanimously indispensable candidates as high-temperature structural materials in aerospace field, in order to improve the thrust weight ratio due to the low density, high specific strength and excellent corrosion resistance [1–3], and also important in other industrial fields such as chemistry, shipping and automobile [4]. However, the inferior anti-creep performance of conventional Ti alloys has limited their application to meet the rigorous requirement. The reason is that most Ti alloy components suffer from high temperature and sustained stress during the service process. The accumulation of creep deformation could finally result in creep rupture of components [5]. A large number of studies have been carried out to comprehend the creep mechanisms and improve creep resistance of Ti alloys. During the creep process at 455 °C/310 MPa, grain boundary sliding appeared to be the primary deformation mechanism for the Ti6Al4V alloy [6]. However, dislocation glide controlled the creep deformation of the commercial pure (CP) Ti alloy at 455 °C/45 MPa [7]. It has been reported that fine grain size could promote grain boundary sliding [8]. For the forged Ti-5Al-5Mo-5V-1Fe-1Cr alloy, the dislocation slip and climb controlled the creep process under the conditions of 400 °C/(200–300) MPa and 500 °C/(200–300) MPa, respectively [9]. The creep process of the forged Ti6Al4V alloy at 600 °C/(97–391) MPa was controlled by dislocation climb [10]. The aforementioned results demonstrated that the creep mechanism for Ti alloys was various under different temperatures and stresses.

In order to enhance creep resistance, traditional methods including increasing grain size of Ti alloys were selected. However, large size led to inferior ductility and limited enhancement of creep resistance. Another method is to develop the titanium matrix composites (TMCs). For example, Ma et al. [11] have investigated the

* Corresponding author.
E-mail address: huanglujun@hit.edu.cn (L.J. Huang).

https://doi.org/10.1016/j.jmst.2019.04.001
1005-0302/

creep behavior of 15 vol.%TiCp/Ti6Al4V composite with a homogeneous distribution of reinforcement between 550 °C and 650 °C. The results showed that the creep resistance of the composite was increased by introducing reinforcement and the stress exponent was decreased by incorporating the threshold stress. The creep mechanism at (16–55) MPa was grain boundary sliding accommodated by the lattice self-diffusion controlled dislocation climb. Lu et al. [12] found that the introduction of TiB, TiC and La_2O_3 reinforcements brought into the threshold stress and stress transfer effect, which were important factors for improving the creep resistance of Ti alloy.

Numerous results showed that tailoring microstructure could effectively improve the mechanical properties. The hierarchical microstructure design demonstrated the possibility of achieving high performance. For example, Wang et al. [13] obtained superior strength and ductility of the stainless steel, due to the collective effect of hierarchically heterogeneous microstructure. An unprecedented tensile ductility has been derived from the Mo alloy with a hierarchical microstructure by Liu et al. [14]. However, most of the previous reports merely focused on the improvement of room-temperature performance. Few researches were about the effect of hierarchical microstructure design on the high temperature property.

In order to improve creep resistance effectively by hindering boundary sliding, one network microstructure was designed by tailoring TiBw distribution around the large Ti6Al4V matrix particle in our previous works [15]. The prepared TiBw/Ti6Al4V composite with the network microstructure has exhibited excellent mechanical properties and increased creep resistance [16]. However, phase boundary sliding was not impeded within the Ti matrix in the TiBw/Ti6Al4V composite. To further improve creep resistance of the composite, blocking phase boundary sliding will be effective and significant. It has been widely recognized that the addition of Si element could significantly improve the creep resistance of Ti alloys [17,18]. In the TiAl alloy, the Si element was found to be beneficial to enhance creep resistance, which was attributed to the formation of fine Ti_5Si_3 precipitate [19]. Learning from the previous work, two-scale network microstructure was designed by precipitating nano-Ti_5Si_3 reinforcement within the β phase to form the second-scale network in the TiBw/Ti6Al4V composite with one-scale network microstructure.

In the present work, the two-scale network structured (Ti_5Si_3+TiBw)/Ti6Al4V composite was successfully fabricated by adding TiB_2 and Si raw material onto Ti6Al4V alloy powder and using powder metallurgy process. In-situ micro-TiBw distributed around large Ti6Al4V matrix particle formed the first-scale network microstructure, while nano-Ti_5Si_3 distributed within the β phase of the matrix formed the second-scale network microstructure. Our previous study verified that the high-temperature tensile properties of the (Ti_5Si_3+TiBw)/Ti6Al4V composite were significantly increased due to the two-scale network microstructure [20]. Considering the pinning effect of the two-scale network microstructure with micro-TiBw and nano-Ti_5Si_3 reinforcements, it is necessary to investigate the creep behavior and anti-creep mechanism of the (Ti_5Si_3+TiBw)/ Ti6Al4V composite.

2. Experimental procedure

In order to significantly enhance creep resistance of titanium matrix composites, the two-scale network microstructure was designed for the (Ti_5Si_3+TiBw)/Ti6Al4V composite. As shown in Fig. 1, the equiaxed "grain boundary" combining with micro-TiBw reinforcement constructed the first-scale network, while the β phase with nano-Ti_5Si_3 reinforcement done the second-scale network. In order to achieve the two-scale microstructure for the

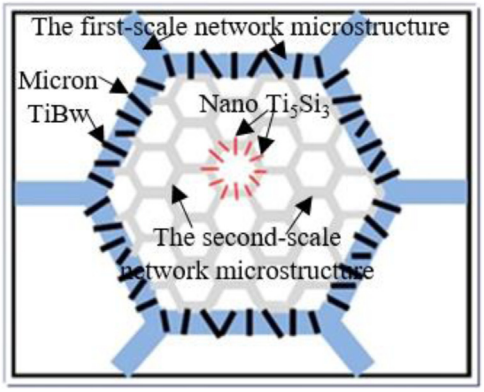

Fig. 1. A schematic illustration of the (Ti_5Si_3+TiBw)/Ti6Al4V composite with two-scale network microstructure.

composite, spherical Ti6Al4V powder (120–150 μm), prismatic TiB_2 powder (1–8 μm) and fine Si powder (1–5 μm) were adopted as raw material. The three powders were blended and low-energy ball milled for 5 h at a speed of 230 rpm under a protective argon atmosphere. The weight ratio of ball to powder was fixed at 5:1. Then the mixed powder was hot pressed in vacuum under a pressure of 20 MPa at 1200 °C and 1.0 h. Afterwards, the compact composite was successfully sintered, which was verified by the microstructure observation and performance test [20–22].

Tensile creep experiment was carried out in air atmosphere using a RWS50 testing machine equipped with load cell and displacement component. Accurate temperature control was guaranteed in the range of ± 2 K, and deformation fluctuation was controlled within 0.5%. The creep data were recorded with an interval of 20 s. Creep tests of the as-sintered composite and Ti6Al4V alloy were performed at 550 °C, 600 °C and 650 °C, and the stress was from 100 MPa to 350 MPa. At lower temperature and stress, the creep test was interrupted even the specimens were not fractured after 100 h, owing to enough steady-state creep information. All the specimens were held for 10 min after reaching the testing temperature, in order to eliminate the effect of temperature inhomogeneity. Dog-bone-shaped specimens with dimension of 10 mm × 5 mm × 2 mm were prepared. After creep test with furnace cooling, the microstructure observation of samples was carried out by using a scanning electron microscope (SEM; ZEISS SUPRA 55 SAPPHIRE) and a transmission electron microscope (TEM; FEI Talos F200x). The composition of the matrix and particle was determined by the energy-dispersive X-ray spectroscopy (EDS). At least ten different positions were performed in each case. TEM specimens were cut and thinned from the regions near the fracture surface of the tested samples.

3. Results and discussion

3.1. Two-scale network microstructure

Microstructures of the as-sintered Ti6Al4V alloy and (Ti_5Si_3+TiBw)/Ti6Al4V composite used for creep test are shown in Fig. 2. The microstructure within the prior-β grain consists of Widmanstätten α-laths in the Ti6Al4V alloy, as shown in Fig. 2(a). The coarse Widmanstätten microstructure of Ti alloys probably leads to high creep resistance and low room-temperature ductility [20,23]. Fig. 2(b)–(d) exhibits that in the as-sintered (Ti_5Si_3+TiBw)/Ti6Al4V composite, TiB whisker (<20 μm) located around the Ti6Al4V matrix particle forms the first-scale network microstructure (about 150 μm), which is an analogous "grain boundary" structure [20–22]. The "grain" size is equal to that of the raw material Ti6Al4V powder. Ti_5Si_3 particle (300–500 nm) distributed within the β

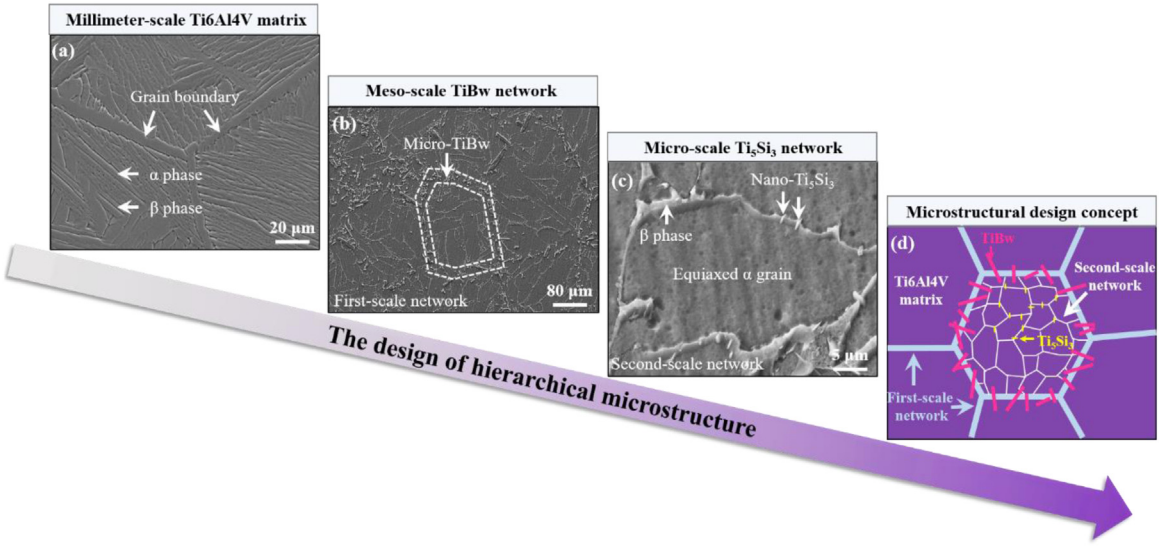

Fig. 2. Microstructure and schematic illustration of the composite. (a) millimeter-scale Ti6Al4V matrix; (b) Meso-scale TiBw network; (c) micro-scale Ti_5Si_3 network; (d) microstructural design concept of the composite.

phase forms the second-scale network microstructure (<30 μm) around the α phase. The first-scale network and the second-scale network construct the two-scale network microstructure with micro-TiBw and nano-Ti_5Si_3 reinforcements in the composite.

3.2. Creep behavior

Fig. 3 shows the creep curves of the Ti6Al4V alloy and (Ti_5Si_3+TiBw)/Ti6Al4V composite when testing at 550 °C and different stresses. The creep test was interrupted when the steady-state stage was obtained after 100 h (labeled as X in Fig. 3(a) and (b)). Firstly, the creep strain is similar to the composites with different TiBw fractions at 200 MPa and 250 MPa, indicating that phase boundary (the second-scale network) sliding dominates the creep deformation, which can be suppressed by nano-Ti_5Si_3 particle, rather than the grain boundary (the first-scale network) sliding. It is worth noting that the creep rate is significantly decreased from $4.44 \times 10^{-8}\ s^{-1}$ to $2.25 \times 10^{-8}\ s^{-1}$, during the steady-state creep stage (stage II) for the (Ti_5Si_3+TiBw)/Ti6Al4V composite at 550 °C/200 MPa. That is to say, the creep resistance of the composite is increased continuously during creep process, which can lead to lower creep rate and creep strain, and longer rupture time. This phenomenon can also be found at 550 °C/250 MPa, as shown in Fig. 3(b). However, it was not observed in the TiBw/Ti6Al4V composite with single network microstructure [16] and in the Ti6Al4V alloy under the identical testing condition. Therefore, it is undoubted that the two-scale network microstructure contributed to the increased creep resistance continuously. Furthermore, the Ti6Al4V alloy rapidly reaches the accelerating stage (stage III), even creep rupture occurs within 16 h, as shown in Fig. 3(b).

Secondly, as shown in Fig. 3(c) and (d), at higher stresses (300 MPa and 350 MPa), both the Ti6Al4V alloy and the composite exhibit typical three creep stages: primary creep (stage I), where the creep rate is decreased with time; steady-state creep (stage II), where the average creep rate is constant; and accelerating creep (stage III), where the creep rate is increased with time. However, the creep rate and creep strain of the composite are significantly decreased, and the rupture time is drastically increased compared with those of the Ti6Al4V alloy. It can be seen from Fig. 3(c) and (d) that the steady-state creep rate of the composite is decreased evidently with increasing TiBw fractions from 1 vol.% to 3.4 vol.%, and this effect is more eminent at higher stress. This phenomenon indicates that grain boundary sliding is the dominant mechanism at higher temperature and stress, which can be hindered by micro-TiBw reinforcement. Similar mechanism was also proven by Singh et al. [24] in the Ti-6Al-4V-B system. Comparing the results in Fig. 3(b) and (d), the steady-state creep rate ($3.71 \times 10^{-7}\ s^{-1}$) of the composite at 350 MPa is much lower than that ($1.37 \times 10^{-6}\ s^{-1}$) of Ti6Al4V alloy at 250 MPa. This result infers that under this condition, constructing two-scale network microstructure leads to an increase in the creep stress (at least 100 MPa).

Thirdly, Table 1 provides a summary of the creep properties extracted from the previous research on various Ti alloys and TMCs. The (Ti_5Si_3+TiBw)/Ti6Al4V composite with two-scale network microstructure in the present study exhibits superior creep resistance over conventional Ti alloys [9,10,23–25] under the similar testing conditions. The rupture time of the (Ti_5Si_3+TiBw)/Ti6Al4V composite is increased by 20 times compared with that of the Ti6Al4V alloy at 550 °C/300 MPa. Moreover, the rupture time is increased by 80 times compared with that of the TiCp/Ti6Al4V composite with conventional homogenous microstructure at 550 °C/300 MPa [11]. Especially, the (Ti_5Si_3+TiBw)/Ti6Al4V composite presents approximately 2 times lower steady-state creep rate than the 8 vol.%TiBw/Ti6Al4V composite with single network microstructure at 550 °C/300 MPa [16]. The results demonstrate that the two-scale network microstructure with nano-Ti_5Si_3 reinforcement can significantly enhance the creep resistance.

As the testing temperature rises up to 600 °C, the rupture time of the (4 vol.%Ti_5Si_3+3.4 vol.%TiBw)/Ti6Al4V composite is more than 6 times longer than that of the Ti6Al4V alloy at 200 MPa, as shown in Fig. 4(a). The steady-state creep rate of the present composite is significantly decreased from $7.28 \times 10^{-7}\ s^{-1}$ to $2.59 \times 10^{-7}\ s^{-1}$, compared with that of the 8 vol.%TiBw/Ti6Al4V composite with single network microstructure [16]. In addition, the creep rupture time of the composite is increased with increasing TiBw fractions, as shown in Fig. 4(b). Furthermore, compared with 5 vol.%TiBw/Ti6Al4V composite under the same creep rupture time [16], the applied stress on the (4 vol.%Ti_5Si_3+3.4 vol.%TiBw)/Ti6Al4V composite can be increased from 200 MPa to 250 MPa (Fig. 4(c)).

The discontinuously reinforced titanium matrix composites (DRTMCs) and Cr-Mo steel are used as structural materials in engineering field. However, 40% of weight reduction can be obtained

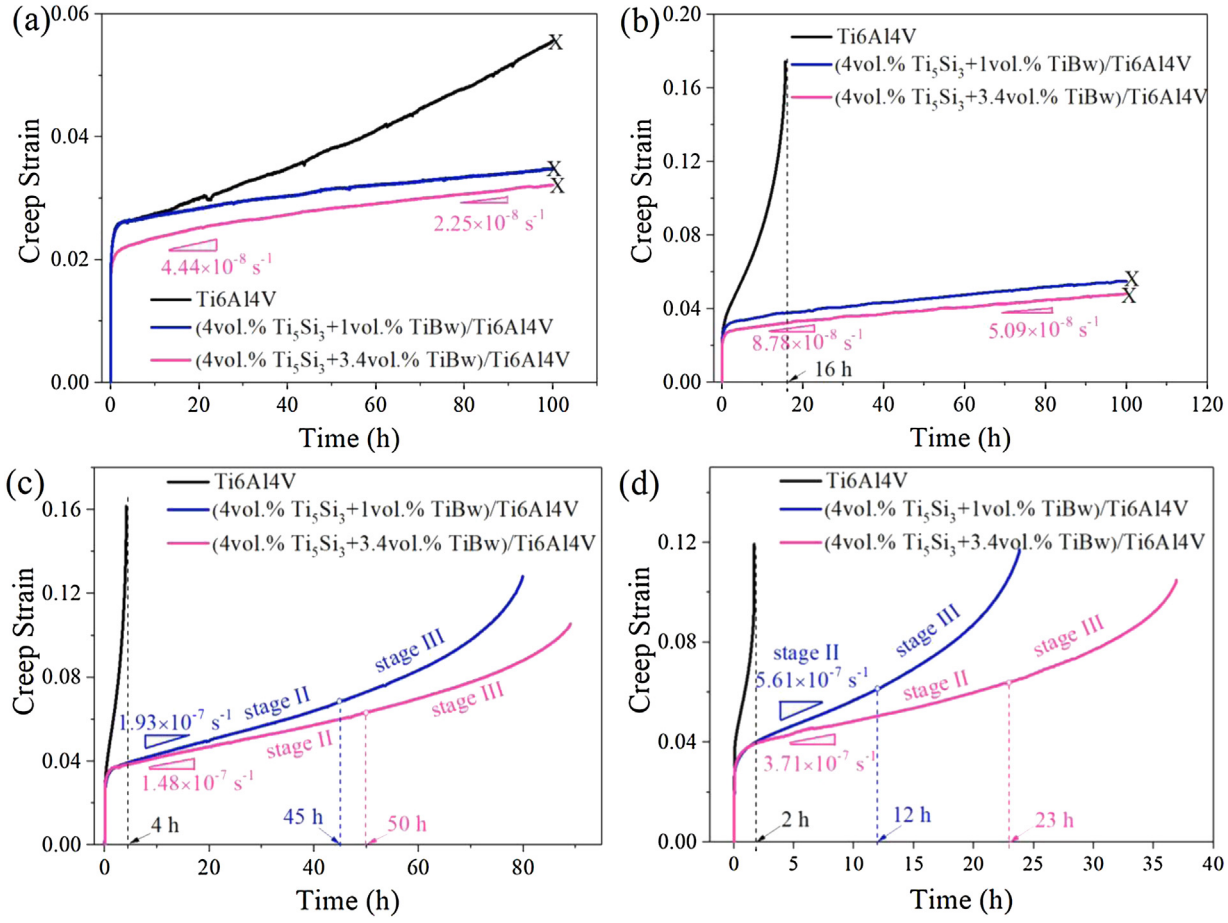

Fig. 3. Creep strain versus time curves of the Ti6Al4V alloy and (Ti_5Si_3+TiBw)/Ti6Al4V composite at: (a) 550 °C/200 MPa; (b) 550 °C/250 MPa; (c) 550 °C/300 MPa; (d) 550 °C/350 MPa.

Table 1
Creep properties of various Ti alloys, conventional TMCs and (Ti_5Si_3+TiBw)/Ti6Al4V composite.

Materials	Ref.	Testing conditions	Steady state creep rate (s^{-1})	Creep rupture time (h)
(4 vol.%Ti_5Si_3+3.4 vol.%TiBw)/Ti6Al4V	This work	550 °C/300 MPa	1.48×10^{-7}	89.0
(4 vol.%Ti_5Si_3+3.4 vol.%TiBw)/Ti6Al4V	This work	550 °C/350 MPa	3.71×10^{-7}	36.0
Ti6Al4V	This work	550 °C/300 MPa	3.73×10^{-6}	4.0
Ti5Al5Mo5V1Fe1Cr(TC18)	[9]	500 °C/300 MPa	4.86×10^{-7}	72.0
Hot-forged Ti6Al4V	[10]	500 °C/361 MPa	9.64×10^{-7}	28.2
Ti6.3Al1.6Zr3.4Mo0.3Si(TC11)	[23]	500 °C/300 MPa	2.83×10^{-7}	–
Ti6Al4V-0.11B	[24]	550 °C/300 MPa	2.25×10^{-6}	7.7
Ti6Al2Sn2Zr2Cr2Mo0.16Si(Ti62222S)	[25]	480 °C/350 MPa	–	50.0
15 vol%TiCp/Ti6Al4V	[11]	550 °C/300 MPa	–	<1.0
8 vol%TiBw/Ti6Al4V	[16]	550 °C/300 MPa	4.06×10^{-7}	20.0

when the high-temperature alloys or steels are replaced by the DRTMCs. Compared with the welded Grade 91 steel, the creep rupture time of the (4 vol.%Ti_5Si_3+3.4 vol.%TiBw)/Ti6Al4V composite is 6 times longer at 200 MPa [26]. The creep stress of the (4 vol.%Ti_5Si_3+3.4 vol.%TiBw)/Ti6Al4V composite is increased by 100 MPa compared with that of the heat-treated 9Cr-1Mo steel [27]. As shown in Fig. 4(c), the creep resistance of the present composite at 250 MPa is at the highest level, compared with that of the TiN-coated Ti6Al4V at 222 MPa [28] as well as the forged Ti6Al4V alloy at 208 MPa [10].

When the creep temperature is elevated to 650 °C, the Ti6Al4V alloy exhibits an extended steady-state creep stage (about 90 h) at the lower stress of 100 MPa. This result could be attributed to coarse Widmanstätten microstructure [29]. However, the (Ti_5Si_3+TiBw)/Ti6Al4V composite exhibits lower creep rate and longer rupture time. Moreover, the continuous decrease of creep rate during the stage II is also observed in Fig. 5(a). The creep strain and creep rate of the composite are remarkably decreased, when compared with those of Ti6Al4V alloy under the same conditions (Fig. 5(b)-(d)). As summarized in Table 2, the (Ti_5Si_3+TiBw)/Ti6Al4V composite possesses superior creep resistance over both the TiBw/Ti6Al4V composite and the engineering steels. Combining with the aforementioned results, one can again deduce that constructing two-scale network microstructure with nano-Ti_5Si_3 reinforcement can significantly enhance the creep resistance in the temperature range of 550–650 °C.

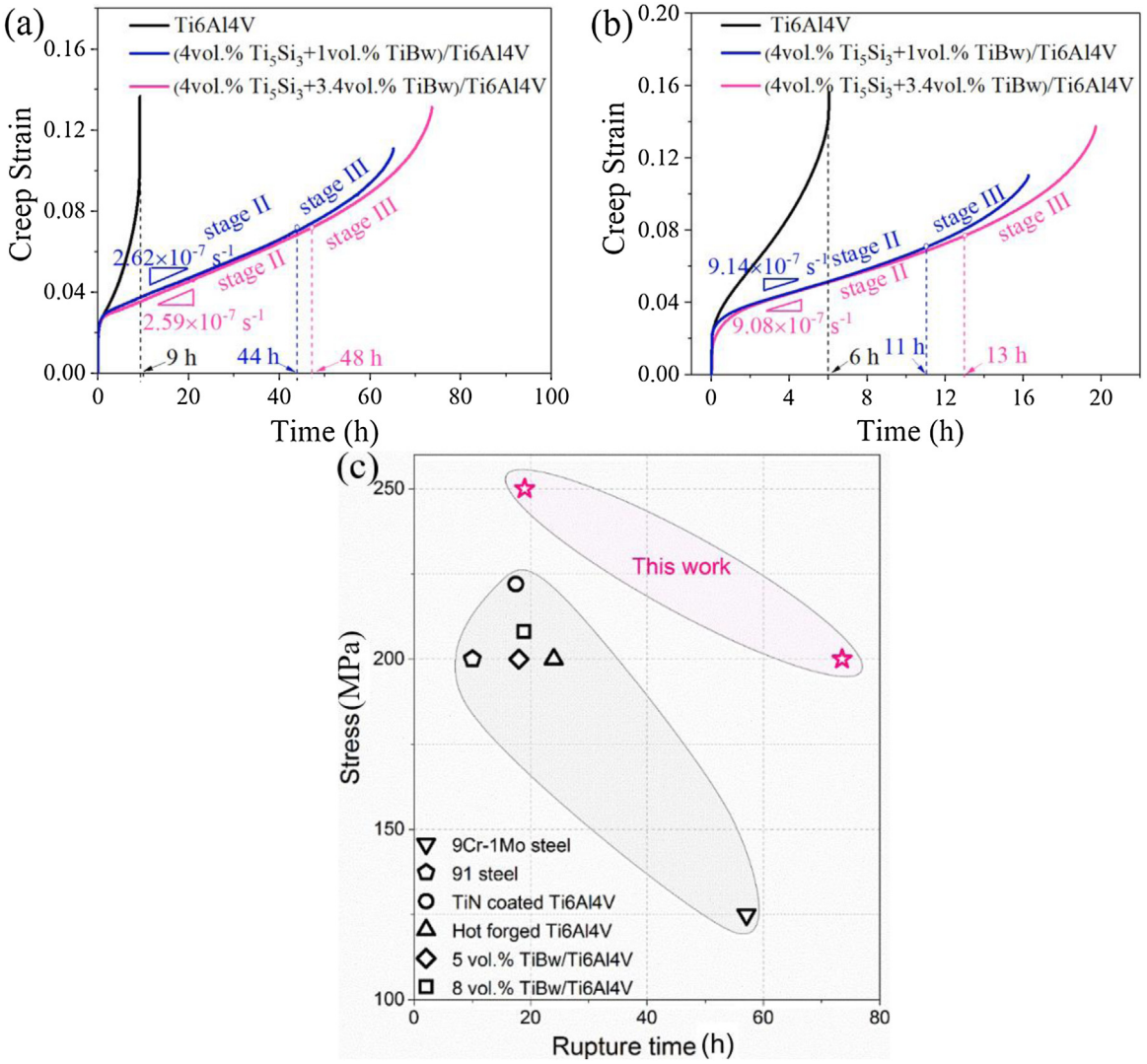

Fig. 4. Creep strain versus time curves of the Ti6Al4V alloy and (Ti_5Si_3+TiBw)/Ti6Al4V composite at 600 °C/200 MPa (a); 600 °C/250 MPa (b); comparison of stress versus rupture time at 600 °C (c) with data from Refs. [10,16,26–28].

3.3. Anti-creep mechanism

Arrhenius equation was adopted by numerous literature to evaluate the creep behavior [12,23]:

$$\dot{\varepsilon} = A\sigma^n \exp\left(\frac{Q/>}{RT}\right) \quad (1)$$

where $\dot{\varepsilon}$, A, σ, Q, R, T and n denote the steady-state creep rate (s^{-1}), material constant, flow stress (MPa), creep activation energy (kJ/mol), gas constant (8.314 J/(mol K)), Kelvin temperature (K) and stress exponent. According to Eq. (1), the kinetic parameters n and Q can be expressed as:

$$n = \left(\frac{\partial \log \dot{\varepsilon}}{\partial \log \sigma}\right)_T \quad (2)$$

$$Q = -R\left(\frac{\partial \ln \dot{\varepsilon}}{\partial (1/T)}\right)_\sigma \quad (3)$$

Fig. 6(a) and (b) shows the plots of logarithmic steady-state creep rate versus logarithmic stress and reciprocal temperature (1000/T) for the Ti6Al4V alloy and (4 vol.%Ti_5Si_3+3.4 vol.%TiBw)/Ti6Al4V composite. The stress exponents calculated from the slopes in Fig. 6(a) are n = 5.2 (550 °C) and n = 5.5 (650 °C) for the Ti6Al4V alloy. Therefore, the anti-creep mechanism is dislocation climb, which is consistent with the study of hot-forged Ti6Al4V alloy in the similar temperature range reported by Badea et al. [30]. It is worth noting that between 200 MPa and 250 MPa at 550 °C, the n value of (4 vol.%Ti_5Si_3+3.4 vol.%TiBw)/Ti6Al4V composite is about 3.0, inferring the presence of the boundary sliding mechanism. It has been reported that the stress exponent of the TiC/Ti6Al4V composite is decreased from (2.4–2.6) to 2 through introducing the threshold stress, and the creep mechanism is boundary sliding. By comparing the different creep rates during the creep stage II, the n value obtained from the lower creep rate is close to 3.7, which indicates that boundary sliding is inhibited and the creep resistance is increased. This is in good agreement with the decrease of the creep rate (Fig. 3). However, when increasing the creep stress to 300 MPa and 350 MPa, the n value is about 6.0, suggesting that dislocation climb is the primary creep mechanism for the composite. For the composite at 650 °C, the stress exponent value is 5.4, which is similar to that of the Ti6Al4V alloy. However, the creep rate in the steady-state stage of the composite is decreased with increasing creep time at lower stress of 100 MPa (Fig. 5(a)).

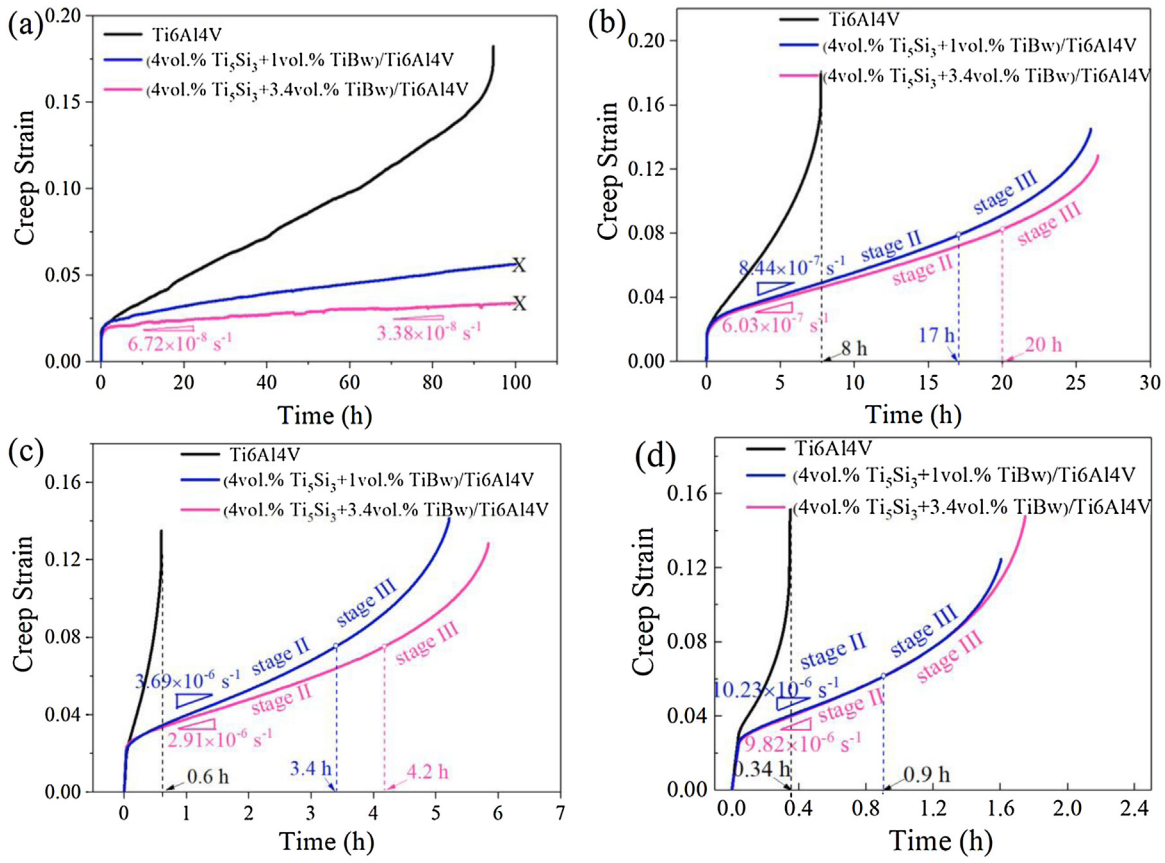

Fig. 5. Creep strain versus time curves of the Ti6Al4V alloy and (Ti_5Si_3+TiBw)/Ti6Al4V composite at: (a) 650 °C/100 MPa; (b) 650 °C/150 MPa; (c) 650 °C/200 MPa; (d) 650 °C/250 MPa.

Table 2
Creep properties of various TMCs and steels at 650 °C.

Materials	Ref.	Testing conditions	Steady state creep rate (s^{-1})	Creep rupture time (h)
(4 vol.%Ti_5Si_3+3.4 vol.%TiBw)/Ti6Al4V	This work	150 MPa	6.03×10^{-7}	26.5
(4 vol.%Ti_5Si_3+3.4 vol.%TiBw)/Ti6Al4V	This work	200 MPa	2.91×10^{-6}	5.5
8 vol%TiBw/Ti6Al4V	[16]	150 MPa	2.55×10^{-6}	14.0
Cast-forged P91 steel	[41]	150 MPa	1.81×10^{-6}	9.3
Cast-forged P91 steel	[41]	200 MPa	4.64×10^{-5}	0.4

The slopes of ln $\dot{\varepsilon}$ -1000/T are corresponding to the creep activation energy Q (Fig. 6(b)). The Q value of the Ti6Al4V alloy is 249.3 kJ/mol at 250 MPa. For the (4 vol.%Ti_5Si_3+3.4 vol.%TiBw)/Ti6Al4V composite, the Q values are 306.8 kJ/mol at 200 MPa and 332.6 kJ/mol at 250 MPa, respectively. Compared with Ti6Al4V alloy, the composite exhibits higher creep activation energy, i.e. higher creep resistance, which demonstrates that dislocation motion and creep strain in the composite would be more difficult due to the blocking effect of two-scale reinforcements in the two-scale network microstructure. Under the conditions of 550 °C/200 MPa and 550 °C/250 MPa, as the creep deformation proceeding, the steady-state creep rate is decreased and the creep activation energy is increased (Fig. 3(a) and (b)), which illustrates that the creep resistance is increased continuously.

The threshold stress (σ_{th}) was introduced to explain higher apparent stress exponents in the DRTMCs [11,12]. According to Ref. [11], the creep data of matrix alloy and composite are plotted as $\dot{\varepsilon}^{1/4.3}$ (corresponding to the dislocation climb process for α-Ti, n = 4.3 and Q = 241 kJ/mol) versus σ, in order to calculate the σ_{th} values (Fig. 6(c)). At the same temperature, the threshold stress (σ_{th}) values of the composite are remarkably higher than that of Ti6Al4V alloy. It is worth noting that the σ_{th} value of the composite at 650 °C is still higher than that of Ti6Al4V alloy at 550 °C. In the temperature range of 550–650 °C, the σ_{th} value of the composite is decreased with respect to the dislocation motion with the help of thermal activation. After compensated with the threshold stress, the steady-state creep rates of the composite (c) and the matrix alloy (m) at 550 °C and 650 °C can be expressed as follows:

$$550^{\circ}C: \dot{\varepsilon}_c = 1.18 \times 10^{-17}(\sigma - 74.5)^{4.3} \quad (4)$$

$$550^{\circ}C: \dot{\varepsilon}_m = 1.16 \times 10^{-16}(\sigma - 21.3)^{4.3}$$

$$650^{\circ}C: \dot{\varepsilon}_c = 7.91 \times 10^{-16}(\sigma - 28.8)^{4.3} \quad (5)$$

$$650^{\circ}C: \dot{\varepsilon}_m = 3.46 \times 10^{-15}(\sigma - 16.0)^{4.3}$$

The above analysis shows that the Q and σ_{th} values of the composite are significantly increased compared with those of the Ti6Al4V alloy under the same condition. That is to say, the

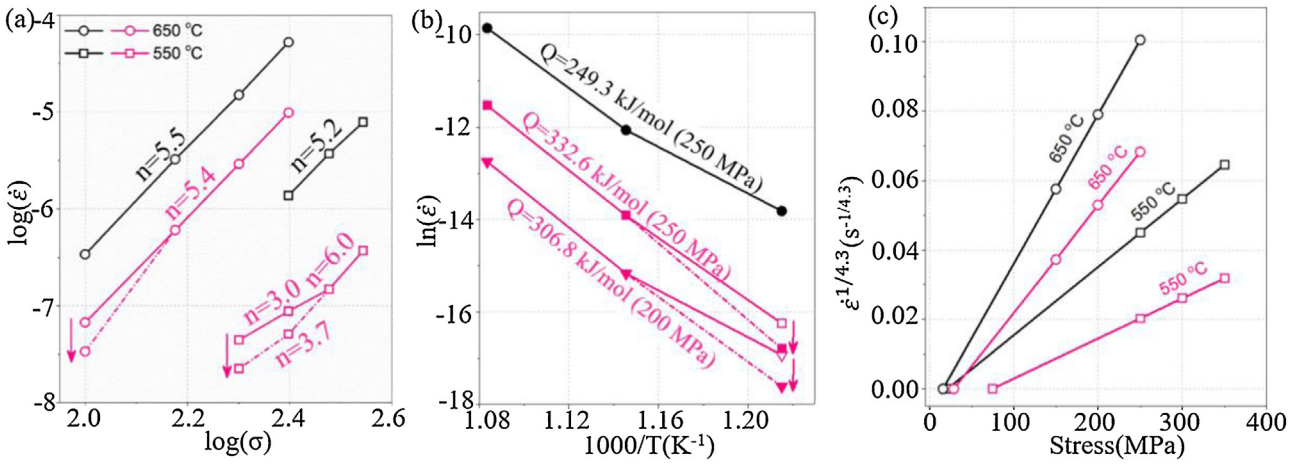

Fig. 6. Logarithmic plots of the steady-state creep rate versus the stress (a) and the reciprocal temperature (b); (c) threshold stresses compensation of Ti6Al4V alloy and (4 vol.%Ti_5Si_3+3.4 vol.%TiBw)/Ti6Al4V composite.

creep resistance of the composite is significantly enhanced by constructing the two-scale network microstructure and nano-Ti_5Si_3 reinforcement.

The observation of the microstructural evolution for materials after creep deformation is important for the analysis of creep mechanism. Fig. 7 shows interior microstructure at 550 °C/250 MPa and fractograph at 650 °C/250 MPa for the (Ti_5Si_3+TiBw)/Ti6Al4V composite and Ti6Al4V alloy. Fig. 7(a) and (b) shows that micro-TiBw reinforcement remains around the Ti6Al4V matrix. That is to say, no obvious microstructure change is presented for the first-scale network. Some micropores distributed in the vicinity of TiBw and the debonded phenomenon between reinforcement and matrix was observed. The deformation compatibility is obvious, due to the long-term creep process. Owing to the fine morphology and higher stress-bearing capacity, the Ti_5Si_3 particle did not break. The fracture of the composite was not observed, which is consistent with the result in Fig. 3. However, a portion of cracks distribute in the α/β interface region with Ti_5Si_3 particle. The reinforcements play a vital role in strengthening, which means that the stress was transferred from matrix to reinforcement. Under the same testing condition (550 °C/250 MPa), void and crack are observed in the Ti6Al4V alloy with inferior creep resistance (Fig. 7(c) and (d)). The α/β lath bending is also noted, indicating that the creep deformation of alloy is large.

As shown in Fig. 7(e) and (f), a predominantly intergranular fracture mode combining with TiBw fracture is presented in the (Ti_5Si_3+TiBw)/Ti6Al4V composite after creep test at 650 °C/250 MPa. Meanwhile, a part of TiB whiskers are pulled out and deboned with the matrix. The fracture of as-sintered Ti6Al4V alloy is intergranular mode and shows many void nucleated at the grain boundary (Fig. 7(g) and (h)). Not only plenty of dimples, but also a mass of voids are observed in the Ti6Al4V alloy, suggesting that the alloy undergoes large creep deformation and the creep resistance is inferior.

Fig. 8 exhibits TEM results of the (4 vol.%Ti_5Si_3+3.4 vol.%TiBw)/Ti6Al4V composite after creep test at 650 °C/250 MPa. Ti_5Si_3 particle is found not only within the β phase but also at the α/β interface (Fig. 8(a) and (b)). Moreover, the size of those distributed within the β phase and at the α/β phase interface are about (100–300) nm and (<100) nm, respectively. Both of them are remarkably smaller than those of the as-sintered composite before creep test. It is well known that the particle refinement is beneficial to improve creep resistance. Therefore, the decrease of creep rate (Figs. 3 and 5) might be related to the evolution of Ti_5Si_3 particle.

High-density dislocation was piled-up and accumulated at interface during creep process. Phase boundary (Fig. 8(c)) and reinforcement (Fig. 8(d)) can play an important role in blocking dislocation motion. Owing to the size difference, the effect of nano-Ti_5Si_3 particle on dislocation is different from that of micro-TiB whisker. The dislocation is pinned around the TiBw reinforcement (Fig. 8(d)). From Fig. 8(e), it can be clearly seen that the long dislocation is bowed out between the nano-Ti_5Si_3 particle. The schematic diagram can clearly exhibit the interaction between dislocation and nano-Ti_5Si_3 particle, as shown in Fig. 8(f). The blue line and black ball denote the dislocation and Ti_5Si_3 particle, respectively. The dislocation can bypass the nano-Ti_5Si_3 particle, due to the small size (<100 nm). As reported, the precipitation acts as obstacle to effectively impede dislocation movement [31]. The dislocation motion is hindered by different forms then the creep resistance is effectively improved. It was well known that the creep behavior can be analyzed according to the occurrence of strain hardening (creep rate is decreased with time) and dynamic recovery softening (creep rate is increased with time) at elevated temperature. During creep process, the strain hardening is controlled by dislocation glide and dislocation interaction with obstacle, such as grain boundary (where formed dislocation wall) and reinforcement. The dynamic recovery softening process is related to dislocation climb and cross slip. As shown in Fig. 8(g), some jogs can be found near the Ti_5Si_3 particle, which indicates that the presence of dislocation interaction during creep deformation process. In addition, the subgrain is formed during recovery process. Therefore, the creep mechanism of the composite at 650 °C/250 MPa should be dislocation climb [23].

In order to further evaluate the Ti_5Si_3 evolution, the STEM images of the (4 vol.%Ti_5Si_3+3.4 vol.%TiBw)/Ti6Al4V composite and the statistical size of Ti_5Si_3 particle within the β phase before and after creep test are displayed in Fig. 9. As shown in Fig. 9(a)-(d), before creep test, most Ti_5Si_3 particles distribute within the β phase. The size of Ti_5Si_3 particle is (300–500) nm, as shown in Fig. 9(h). However, after creep test (Fig. 9(e)-(f)), the amount of Ti_5Si_3 particles distributed within the β phase is reduced and the size is decreased to (100–300) nm (Fig. 9(i)). Furthermore, the composition of the Ti matrix and Ti_5Si_3 particle is presented in Fig. 10. The Si content is increased in the Ti matrix, and decreased in the Ti_5Si_3 particle after creep test. These phenomena indicate that Ti_5Si_3 is dissolved, due to the ripening effect controlled by Si element diffusion at high temperature and external stress, then precipitated at α/β phase boundary region by smaller-sized particle during creep process (Fig. 8). According to Ostwald ripening theory, small precipitate could dissolve controlled by element diffusion in

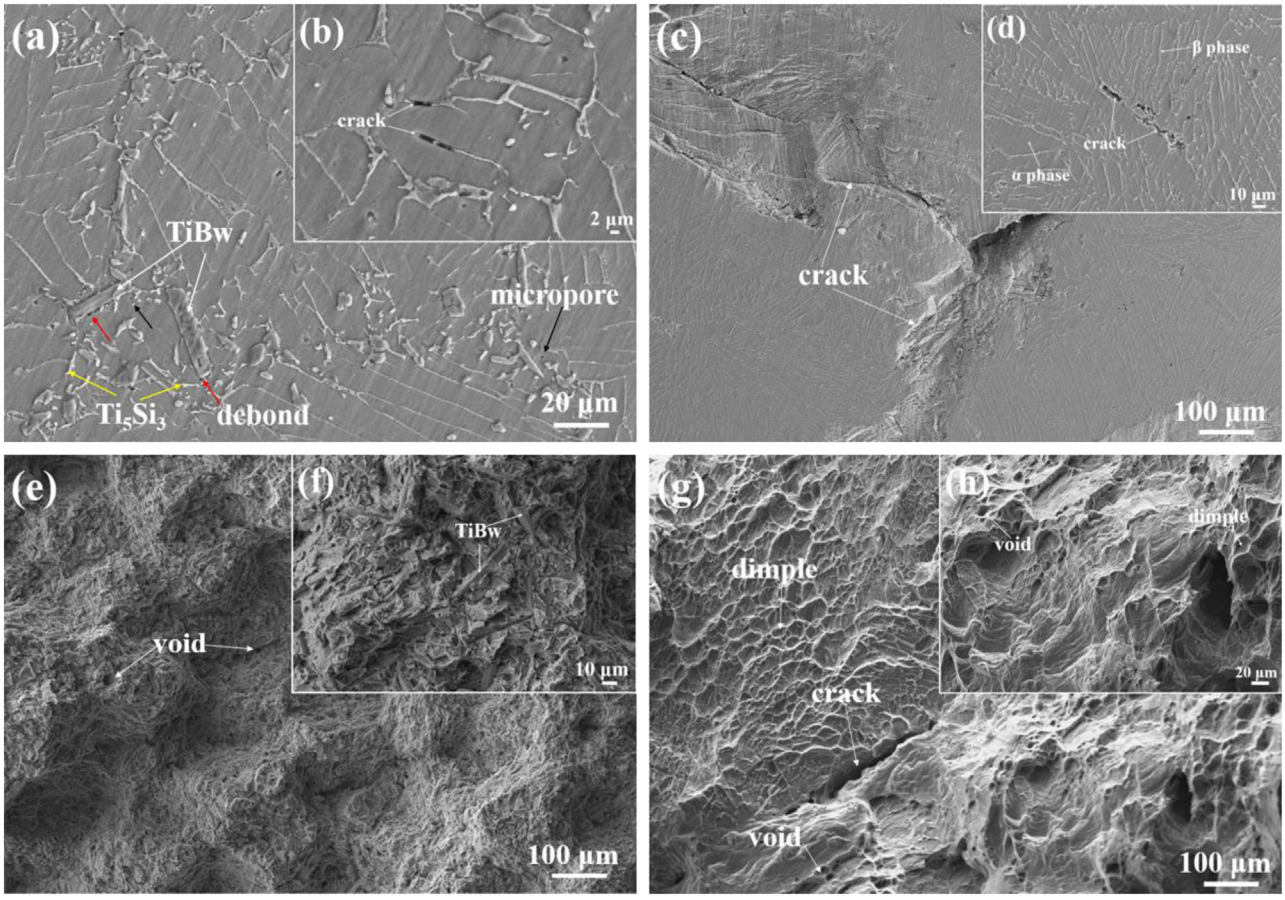

Fig. 7. Interior microstructure of the (4 vol.%Ti_5Si_3+3.4 vol.%TiBw)/Ti6Al4V composite (a and b) and the Ti6Al4V alloy (c and d) at 550 °C/250 MPa; the fractograph of the composite (e and f) and alloy (g and h) after creep test at 650 °C/250 MPa.

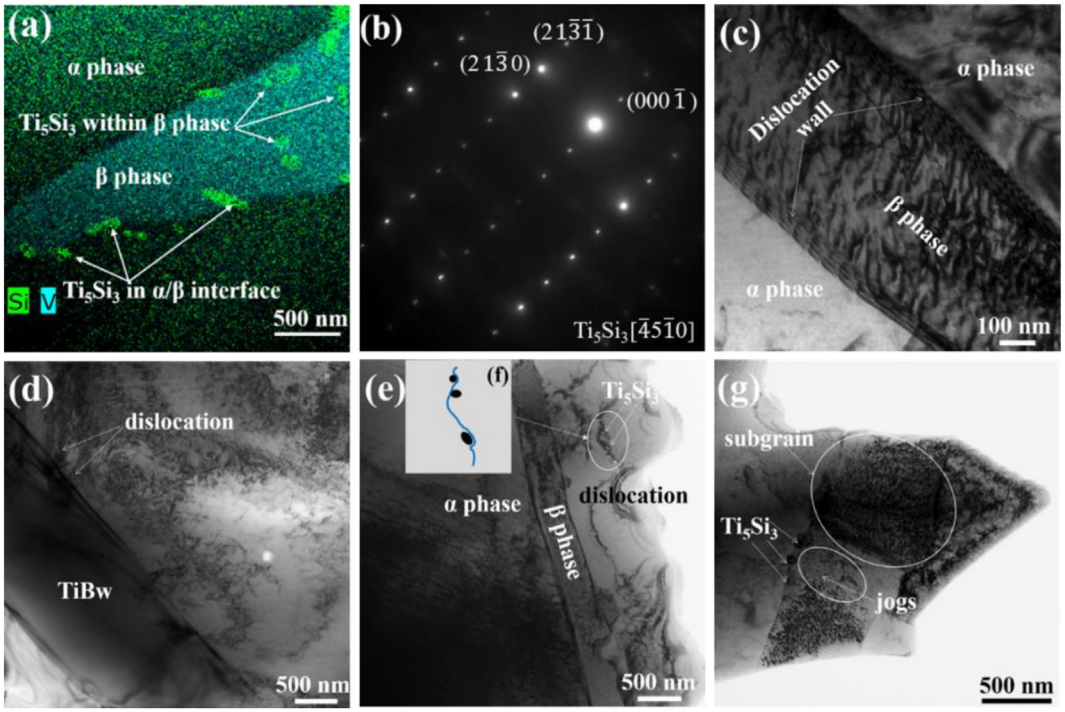

Fig. 8. TEM results taken from the (4 vol.%Ti_5Si_3+3.4 vol.%TiBw)/Ti6Al4V composite at 650 °C/250 MPa. (a) the high-angle annular dark-field (HAADF) scanning TEM (STEM) image; (b) the selected area electron diffraction pattern (SADP) of Ti_5Si_3; (c)-(g) TEM micrographs of dislocation configuration.

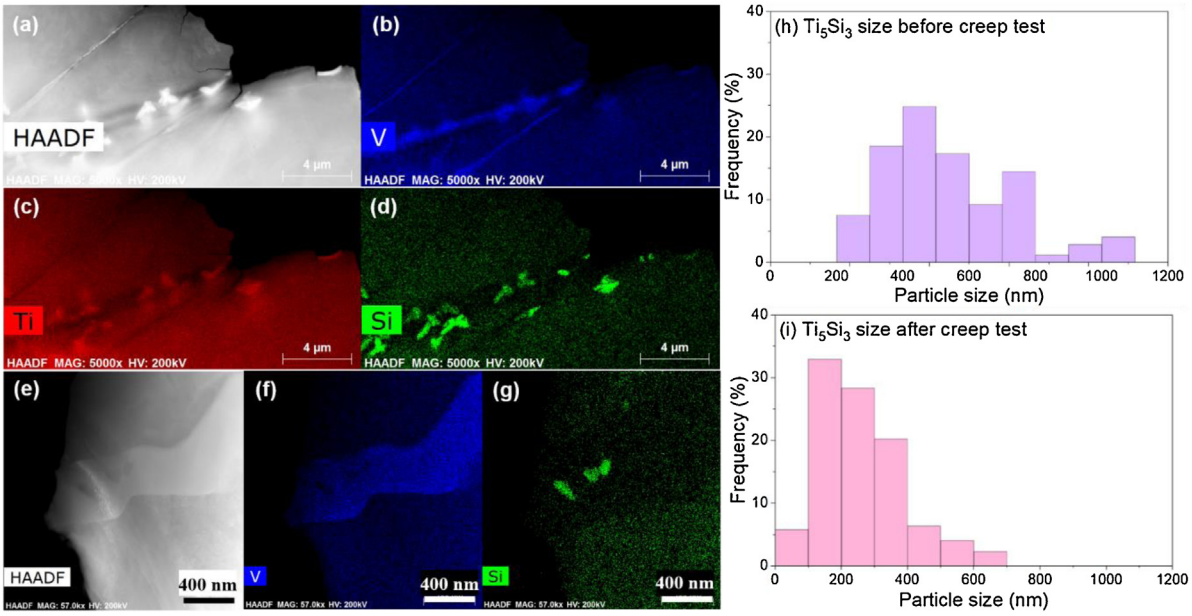

Fig. 9. High-angle annular dark-field (HAADF) scanning TEM (STEM) images of the (Ti_5Si_3+TiBw)/Ti6Al4V composite before (a–d) and after (e–g) creep test at 650 °C/250 MPa; The statistical size of Ti_5Si_3 particle within β phase before (h) and after (i) creep test.

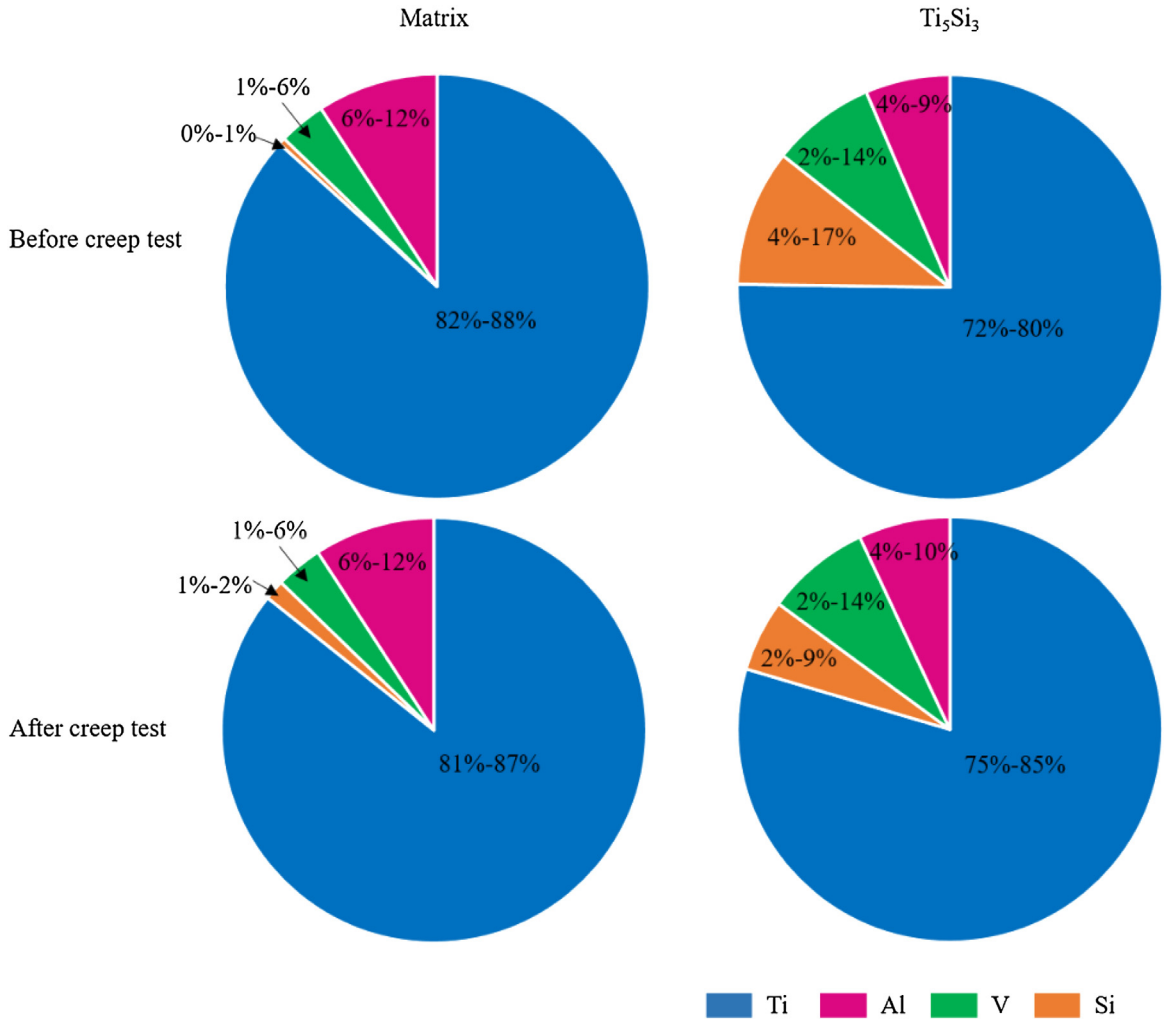

Fig. 10. Composition (at.%) of the Ti matrix and Ti_5Si_3 particle for samples before and after creep test.

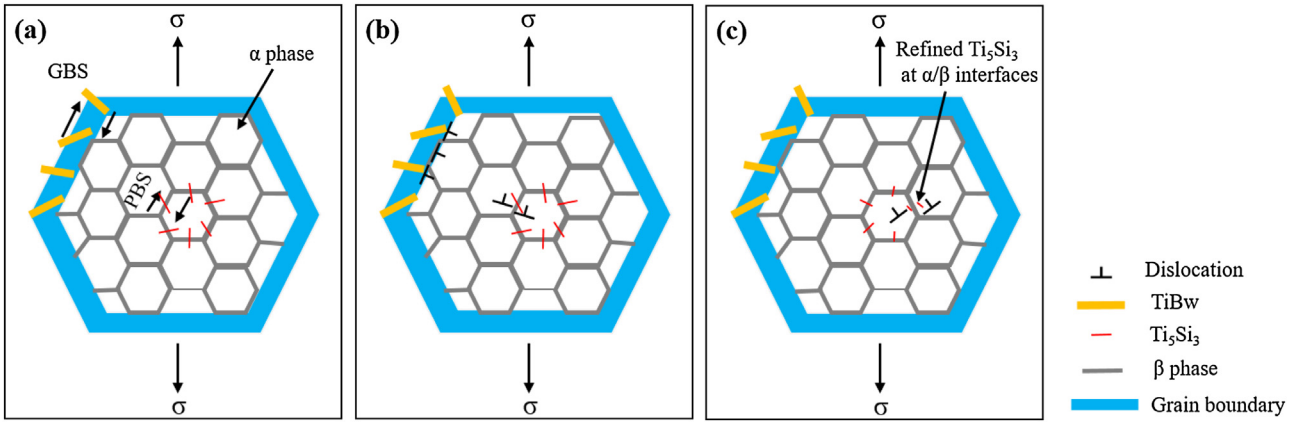

Fig. 11. A schematic illustration of anti-creep mechanism of the (Ti_5Si_3+TiBw)/Ti6Al4V composite during creep test. (a) grain and phase boundary sliding; (b) dislocation piled-up upon grain and phase boundary region; (c) refined Ti_5Si_3 particle distributed at α/β interface.

multicomponent alloys [32,33]. Previous literature also reported similar dissolution phenomenon of precipitate at high temperature and external stress. For example, during the isothermal compression deformation of Inconel 718 alloy at temperature of 950 °C and strain rate of 0.005 s^{-1}, the spheroidization of plate-like Ni_3Nb phase occurred, due to the effect of deformation breakage and dissolution breakage [34]. The dissolution of Ni_3Nb phase was also found in the GH4169 superalloy during isothermal compression test [35].

Owing to the limited solubility of Si in the β-Ti matrix, when Si content exceeds the critical solid solubility, the Ti_5Si_3 phase precipitates in the α/β interface region, since the Si atom prefers to segregate at interface with high-density dislocation after long-time creep process. In previous literature [36,37], Si atom could precipitate as silicide state during the process of high-temperature exposure or creep. Viswanathan et al. [37] found that the Ti_5Si_3 precipitated at the α/β interface in the Ti-6Al-2Sn-4Zr-2Mo alloy during creep test at 565 °C/310 MPa. The precipitate was then interacted with dislocation during creep deformation, which contributed to the improved creep strength of Ti alloy. In addition, the β stabilizer (V element) was mainly distributed in the β phase. The repulsion between Si and V element could push the Si atom out of the β phase such that the Si atom accumulated at the α/β phase boundary, which can probably enhance the creep resistance of the composite by silicide precipitate impeding the slip of phase boundary [5].

Fig. 11 shows a schematic illustration of the anti-creep mechanism of the (Ti_5Si_3+TiBw)/Ti6Al4V composite during creep test. TiBw in the first-scale network boundary region can act as barrier to block grain boundary sliding (GBS). Ti_5Si_3 in the α/β phase interface can impede phase boundary sliding (PBS). Both of the ceramic reinforcements can hinder dislocation motion. The dislocation is piled-up at grain boundary or interface. It was reported that the silicide presenting on or along the lath interface could act as barrier to the creep deformation along lath interface [31]. The precipitated Ti_5Si_3 phase could impede the slip of dislocation and grain boundary [38,39]. In Si-bearing alloys, the interaction between dislocation and precipitate could lead to the decrease in the primary and secondary creep rates [37]. In addition, the refinement of Ti_5Si_3 precipitation could result in the increase of creep resistance [23]. Yu et al. [40] studied the impact of pre-weld tempering temperature on creep behavior of the Grade 91 Cr-Mo steel. The dissolution and re-precipitation of $M_{23}C_6$ grain improved the creep property by pinning boundary and preventing recrystallization.

Based on the result and analysis above, the superior creep resistance of the present (Ti_5Si_3+TiBw)/Ti6Al4V composite can be attributed to the two-scale network microstructure and two-scale reinforcements. Moreover, during creep process, the dissolution and refinement of nano-Ti_5Si_3 plays a crucial role in improving the creep resistance of the composite. Therefore, the phase boundary sliding is effectively hindered and then the creep resistance is significantly enhanced during creep stage by the two-scale network microstructure with nano-Ti_5Si_3 reinforcement.

4. Conclusions

The two-scale network microstructure with nano-Ti_5Si_3 reinforcement was constructed for titanium matrix composites, and the superhigh creep resistance and anti-creep mechanism were exploited in the present study. Based on the investigation, the following conclusions can be drawn:

(1) The two-scale network microstructure with nano-Ti_5Si_3 reinforcement was successfully constructed by powder metallurgy combining with in-situ synthesis and precipitation in the (Ti_5Si_3+TiBw)/Ti6Al4V composite, which achieved a superhigh creep resistance. Compared with the Ti6Al4V alloy, the rupture time of the composite could be increased by 20 times at 550 °C/300 MPa.

(2) During creep process at high temperature and external stress, the nano-Ti_5Si_3 particle with (300–500) nm was dissolved, and smaller nano-Ti_5Si_3 particle (100–300 nm) precipitated near the α/β interface due to Si element diffusion, which could continuously enhance the creep resistance and decrease the creep rate of the composite.

(3) The superhigh creep resistance of the (Ti_5Si_3+TiBw)/Ti6Al4V composite could be attributed to the following roles: the two-scale network microstructure could effectively block grain boundary sliding and phase boundary sliding, respectively; the two-scale reinforcements could effectually impede dislocation motion; the refined Ti_5Si_3 particle could further increase the inhibiting role.

Acknowledgements

This work is financially supported by the National Key R&D Program of China (No. 2017YFB0703100), the National Natural Science Foundation of China (NSFC) under Grant Nos. 51822103, 51671068

and 51731009, and the Fundamental Research Funds for the Central Universities (No. HIT.BRETIV.201902).

References

[1] A. Devaraj, V.V. Joshi, A. Srivastava, S. Manandhar, V. Moxson, V.A. Duz, C. Lavender, Nat. Commun. 7 (2016) 11176.
[2] Y.M. Ren, X. Lin, X. Fu, H. Tan, J. Chen, W.D. Huang, Acta Mater. 132 (2017) 82–95.
[3] S.J. Wolff, S. Lin, E.J. Faierson, W.K. Liu, G.J. Wagner, J. Cao, Acta Mater. 132 (2017) 106–117.
[4] D. Banerjee, J.C. Williams, Acta Mater. 61 (2013) 844–879.
[5] Y. Li, Y. Chen, J.-R. Liu, Q.-M. Hu, R. Yang, Sci. Rep. 6 (2016) 30611.
[6] H. Li, C.J. Boehlert, T.R. Bieler, M.A. Crimp, Philos. Mag. 95 (2015) 691–729.
[7] H. Li, D.E. Mason, Y. Yang, T.R. Bieler, M.A. Crimp, C.J. Boehlert, Philos. Mag. 93 (2013) 2875–2895.
[8] I.G. Dastidar, V. Khademi, T.R. Bieler, A.L. Pilchak, M.A. Crimp, C.J. Boehlert, Mater. Sci. Eng. A 636 (2015) 289–300.
[9] X.A. Nie, Z. Hu, H.Q. Liu, D.Q.-q. Yi, T.Y. Chen, B.F. Wang, Q. Gao, D.C. Wang, Mater. Sci. Eng. A 613 (2014) 306–316.
[10] M.J.R. Barboza, C. Moura Neto, C.R.M. Silva, Mater. Sci. Eng. A 369 (2004) 201–209.
[11] Z.Y. Ma, R.S. Mishra, S.C. Tjong, Acta Mater. 50 (2002) 4293–4302.
[12] L. Xiao, W. Lu, J. Qin, Y. Chen, D. Zhang, M. Wang, F. Zhu, B. Ji, Compos. Sci. Technol. 69 (2009) 1925–1931.
[13] Y.M. Wang, T. Voisin, J.T. McKeown, J. Ye, N.P. Calta, Z. Li, Z. Zeng, Y. Zhang, W. Chen, T.T. Roehling, R.T. Ott, M.K. Santala, P.J. Depond, M.J. Matthews, A.V. Hamza, T. Zhu, Nat. Mater. 17 (2018) 63–71.
[14] G. Liu, G.J. Zhang, F. Jiang, X.D. Ding, Y.J. Sun, J. Sun, E. Ma, Nat. Mater. 12 (2013) 344–350.
[15] L.J. Huang, L. Geng, H.X. Peng, Prog. Mater. Sci. 71 (2015) 93–168.
[16] S. Wang, L.J. Huang, L. Geng, F. Scarpa, Y. Jiao, H.X. Peng, Sci. Rep. 7 (2017) 40823.
[17] M. Es-Souni, Mater. Charact. 46 (2001) 365–379.
[18] M.R. Winstone, R.D. Rawlings, D.R.F. West, J. Less-Common Met. 39 (1975) 205–217.
[19] T. Klein, L. Usategui, B. Rashkova, M.L. Nó, J. San Juan, H. Clemens, S. Mayer, Acta Mater. 128 (2017) 440–450.
[20] Y. Jiao, L.J. Huang, S. Wang, X.T. Li, Q. An, X.P. Cui, L. Geng, J. Alloys. Compd. 704 (2017) 269–281.
[21] Y. Jiao, L.J. Huang, T.B. Duan, S.L. Wei, B. Kaveendran, L. Geng, Sci. Rep. 6 (2016) 32991.
[22] Y. Jiao, L.J. Huang, Q. An, S. Jiang, Y.N. Gao, X.P. Cui, L. Geng, Mater. Sci. Eng. A 673 (2016) 595–605.
[23] Y. Gu, F. Zeng, Y. Qi, C. Xia, X. Xiong, Mater. Sci. Eng. A 575 (2013) 74–85.
[24] G. Singh, D.V.V. Satyanarayana, R. Pederson, R. Datta, U. Ramamurty, Mater. Sci. Eng. A 597 (2014) 194–203.
[25] J. Koike, K. Maruyama, Mater. Sci. Eng. A 263 (1999) 155–159.
[26] T. Shrestha, M. Basirat, S. Alsagabi, A. Sittiho, I. Charit, G.P. Potirniche, Mater. Sci. Eng. A 669 (2016) 75–86.
[27] B.K. Choudhary, Mater. Sci. Eng. A 585 (2013) 1–9.
[28] V.M.C.A. Oliveira, A.M. Vazquez, C. Aguiar, A. Robin, M.J.R. Barboza, Mater. Sci. Eng. A 670 (2016) 357–368.
[29] M.J.R. Barboza, E.A.C. Perez, M.M. Medeiros, D.A.P. Reis, M.C.A. Nono, F.P. Neto, C.R.M. Silva, Mater. Sci. Eng. A 428 (2006) 319–326.
[30] L. Badea, M. Surand, J. Ruau, B. Viguier, Univ. Polytech. Buchar. Sci. Bull. 76 (2014) 185–196.
[31] Y.W. Kim, S.L. Kim, Intermetallics 53 (2014) 92–101.
[32] Z. Sun, G. Song, J. Ilavsky, G. Ghosh, P.K. Liaw, Sci. Rep. 5 (2015) 16081.
[33] T. Philippe, P.W. Voorhees, Acta Mater. 61 (2013) 4237–4244.
[34] H.Y. Zhang, S.H. Zhang, M. Cheng, Z.X. Li, Mater. Charact. 61 (2010) 49–53.
[35] Y. Ning, M.W. Fu, X. Chen, Mater. Sci. Eng. A 540 (2012) 164–173.
[36] P. Davies, R. Pederson, M. Coleman, S. Birosca, Acta Mater. 117 (2016) 51–67.
[37] G.B. Viswanathan, S. Karthikeyan, R.W. Hayes, M.J. Mills, Acta Mater. 50 (2002) 4965–4980.
[38] D.O. Poletaev, A.G. Lipnitskii, A.I. Kartamyshev, D.A. Aksyonov, E.S. Tkachev, S.S. Manokhin, M.B. Ivanov, Y.R. Kolobov, Comput. Mater. Sci. 95 (2014) 456–463.
[39] C. Colinet, J.C. Tedenac, Intermetallics 18 (2010) 1444–1454.
[40] X. Yu, S.S. Babu, H. Terasaki, Y. Komizo, Y. Yamamoto, M.L. Santella, Acta Mater. 61 (2013) 2194–2206.
[41] C. Pandey, M.M. Mahapatra, P. Kumar, R.S. Vidyrathy, A. Srivastava, Mater. Sci. Eng. A 695 (2017) 291–301.